2D Materials

PAPER

Atomistic mechanisms of seeding promoter-controlled growth of molybdenum disulphide

Hayoung Ko[1,2], Han Seul Kim[3], Muhammad Sufyan Ramzan[3], Seongjae Byeon[3], Soo Ho Choi[4], Ki Kang Kim[2,5], Yong-Hoon Kim[3] and Soo Min Kim[1]

1   Institute of Advanced Composite Materials, Korea Institute of Science and Technology (KIST), San101 Eunha-Ri, Bongdong-Eup, Wanju-Gun, Jeonbuk, 55324, Republic of Korea
2   Department of Energy Science, Sungkyunkwan University, Suwon, 16419, Republic of Korea
3   School of Electrical Engineering and Graduate School of EEWS, Korean Advanced Institute of Science and Technology (KAIST), 291 Deahak-ro, Yuseong-gu, Daejeon, 34141, Republic of Korea
4   Department of Physics, Dongguk University, Seoul, 04620, Republic of Korea
5   Center for Integrated Nanostructure Physics (CINAP), Institute for Basic Science (IBS), Suwon, 16419, Republic of Korea

E-mail: y.h.kim@kaist.ac.kr and smkim@kist.re.kr

Abstract

Seeding promoters facilitate the nucleation and growth of transition metal dichalcogenides in chemical vapor deposition (CVD). However, sophisticated roles of seeding promoter remain unclear. Here, adopting triangular-shaped crystal violet (CV) consisting of nonpolar and polar parts as the seeding promoter, we study the role of seeding promoter for the growth of molybdenum disulfide (MoS_2). We systematically control the geometrical configuration of CV on SiO_2/Si substrate by changing the solvent polarity and find that it strongly affects the growth of monolayer or multilayer MoS_2 domains via CVD. Monolayer MoS_2 domains were predominantly grown on randomly lying-down CV configurations on SiO_2/Si substrate, whereas multilayer MoS_2 domains are synthesized at concentrated polar parts in CV micelle on the substrate. Density functional theory calculations reveal that the initial nucleation step for the MoS_2 growth is the adsorption of S on CV and the most favourable S adsorption site is the polar part in CV. Furthermore, it is found that the CV adsorption to SiO_2 is mediated by the polar CV part and additionally strengthened in the lying-down CV configuration. Enhancing the thermal stability as well as hindering the re-aggregation of CV at high temperature, the lying down CV configuration allows the predominant growth of monolayer MoS_2. This work provides a general framework to understand the growth of MoS_2 from aromatic seeding promoters.

1. Introduction

Transition metal dichalcogenides (TMdCs, MX_2 (M = Mo, W; X = S, Se) have been highlighted as promising two-dimensional (2D) van der Waals materials due to their unique physical and chemical properties such as tightly-bound excitons, strong spin–orbit coupling, and gigantic magnetoresistance [1, 2]. In particular, their energy band gaps in visible range together with high carrier mobility enable various electronic and optoelectronic applications such as high speed switching device and solar cell [3–5]. Among TMdCs, molybdenum disulphide (MoS_2) exhibits the highest carrier mobility with the lowest effective mass [6–8], and accordingly many researches have been carried out on its fundamental properties and device applications [9, 10]. However, most studies

remain at the proof-of-concept level, owing to the absence of a reliable growth technique to produce large-area and high-quality MoS_2 film.

Among several methods [11–14], chemical vapour deposition (CVD) is known to be the most promising method for the growth of large-area MoS_2 films due to its high throughput, scalability, and low cost [15–20]. MoS_2 growth in CVD proceeds in the following steps: (1) supply of precursors into CVD furnace, (2) adsorption and diffusion of precursors on the growth substrate, and (3) nucleation and growth of MoS_2 [15–20]. To achieve high-quality and large-area MoS_2, all growth procedures associated with kinetics and thermodynamics as well as precursor and substrate should be optimized. As an important variable for the growth of MoS_2 films, diverse growth substrates have been investigated [21–24]. Insulating substrates

such as silicon dioxide, hexagonal boron nitride, mica, glass, and sapphire are typically utilized rather than catalytic metal substrates because most metals except gold can react with sulphur to form metal-sulphur compound or with molybdenum to make metal-alloy [25–27]. Although gold is an ideal substrate for the growth of MoS$_2$ or other TMdCs, the high price of gold hinders its usage for commercial applications [28, 29]. Therefore, insulating substrates are inevitably used for the growth of MoS$_2$. Some studies have demonstrated direct growth of MoS$_2$ on insulating substrate. However, it needs high flux of precursor by evaporating solid phase precursors of molybdenum trioxides (MoO$_3$) and sulphur (S) powders via local heating which degrades reproducibility for MoS$_2$ growth due to the uncontrollable vapour pressure of precursors. Recently, reliable precursors of volatile molybdenum carbonyl and liquid diethyl sulphide have been developed. The problem is that low adsorption of precursor on the substrate extends growth time up to ~24 h to reach complete MoS$_2$ film [30].

To increase the adsorption of precursors on growth substrate, a seeding promoter such as perylene 3,4,9,10-tetracarboxylic acid tetrapotassium salt (PTAS) or graphene oxide has been introduced. After deposition of the seeding promoter on the insulating substrate, reproducibility of the growth of MoS$_2$ film and its quality are much improved [31]. Moreover, the growth time dramatically decreases within few minutes, similar to that of other 2D family such as graphene and hexagonal boron nitride [32, 33]. The quality of MoS$_2$ is also influenced by the kind of seeding molecules [34]. For example, among various seeding promoters including PTAS, copper phthalocyanine and crystal violet (CV), MoS$_2$ grown on PTAS exhibits the highest electrical mobility and good optical property. However, while it is known that it facilitates the growth of MoS$_2$, detailed roles of the seeding promoters have not been revealed yet.

Here, adopting the triangular-shape crystal violet (CV) as the seed molecule and carrying out a combined experimental and theoretical analysis, we systematically study the role of seeding promoter for the growth of MoS$_2$. The CV molecule consists of nonpolar (hydrophobic) and polar (hydrophilic) parts, enabling the control of CV configuration on the substrate by using solvents with different polarity. To observe the growth behaviour of MoS$_2$, the following three configurations were prepared in different solvents: (1) polar parts concentrated to the centre of CV micelle, (2) nonpolar parts concentrated to the centre of CV micelle, and (3) randomly distributed CV molecules. After spin-coating of each CV solution onto SiO$_2$, we obtained markedly different growth modes of MoS$_2$. Monolayer MoS$_2$ domains were predominantly grown from the configuration (3) of randomly distributed CV molecules, whereas multilayer MoS$_2$ domains were synthesized from the configuration (1) of concentrated CV polar parts. On the other hand, growth of

MoS$_2$ was not observed from the configuration (2) of concentrated CV nonpolar parts. Density functional theory (DFT) calculations are performed to clarify the detailed roles of CV for the growth of MoS$_2$. It is found that the polar part of CV provides a preferred site for S adsorption, initiating the nucleation for MoS$_2$ growth. Moreover, it is found that the binding of CV to the SiO$_2$ surface is mediated by the CV polar part and furthermore strongly enhanced in the lying-down CV configuration. We deduce that the lying-down and standing-up configurations of CV with their polar parts contacting the SiO$_2$ surface should result in the monolayer and multilayer MoS$_2$ growth, respectively. We thus demonstrate that the geometrical configuration of polar part in seeding promoters with respect to the substrate surface is a determining factor for the TMdCs growth behaviour.

2. Results and discussion

Triangular CV consists of hydrophobic nonpolar and hydrophilic polar parts (figure 1(a)). The polar part was induced by placing chloride ion (Cl$^-$) next to N$^+$ site in CV. We engineered the configuration of CV by varying the polarity of solvent with different ratios of water and isopropanol (IPA) [35]. Nonpolar and polar parts should be concentrated to the centre of CV micelle in water and IPA, respectively (denoted as water-CV and IPA-CV, respectively). On the other hand, individual CV molecules should be dissolved or polar and nonpolar parts should be randomly distributed in the bisolvent mixture of water and IPA (a volume ratio of 1:4 was adopted; denoted as bisolvent-CV) (figure 1(b)) [35]. The appearance of CV in different solvents was similar by showing violet colour (figure 1(c)). This indicates that CV in micelle or molecular forms are well dissolved regardless of the type of solvent.

After spin coating different CV solutions onto the SiO$_2$/Si substrate, we observed different surface morphologies depending on the ratio of water and IPA (figures S1(a)–(c), supplementary information (stacks. iop.org/TDM/7/015013/mmedia)). First, some CV stains with few particles were observed from water-CV solution, and this poor deposition indicates that CV micelles exposing hydrophobic nonpolar parts are weakly adsorbed on SiO$_2$. On the other hand, lots of hemisphere-shaped dots were observed from IPA-CV solution, indicating that CV micelles were well anchored on SiO$_2$ in monolayer configurations. Finally, the surface obtained from bisolvent-CV was much smoother than others, indicating randomly distributed and strongly adsorbed CV molecules. We will provide below more detailed analysis of CV adsorption conformations and their strengths based on theoretical calculation results.

To grow MoS$_2$ on different surface morphologies, conventional two-zone CVD method was exploited. Thermally evaporated MoO$_3$ film and S powder were
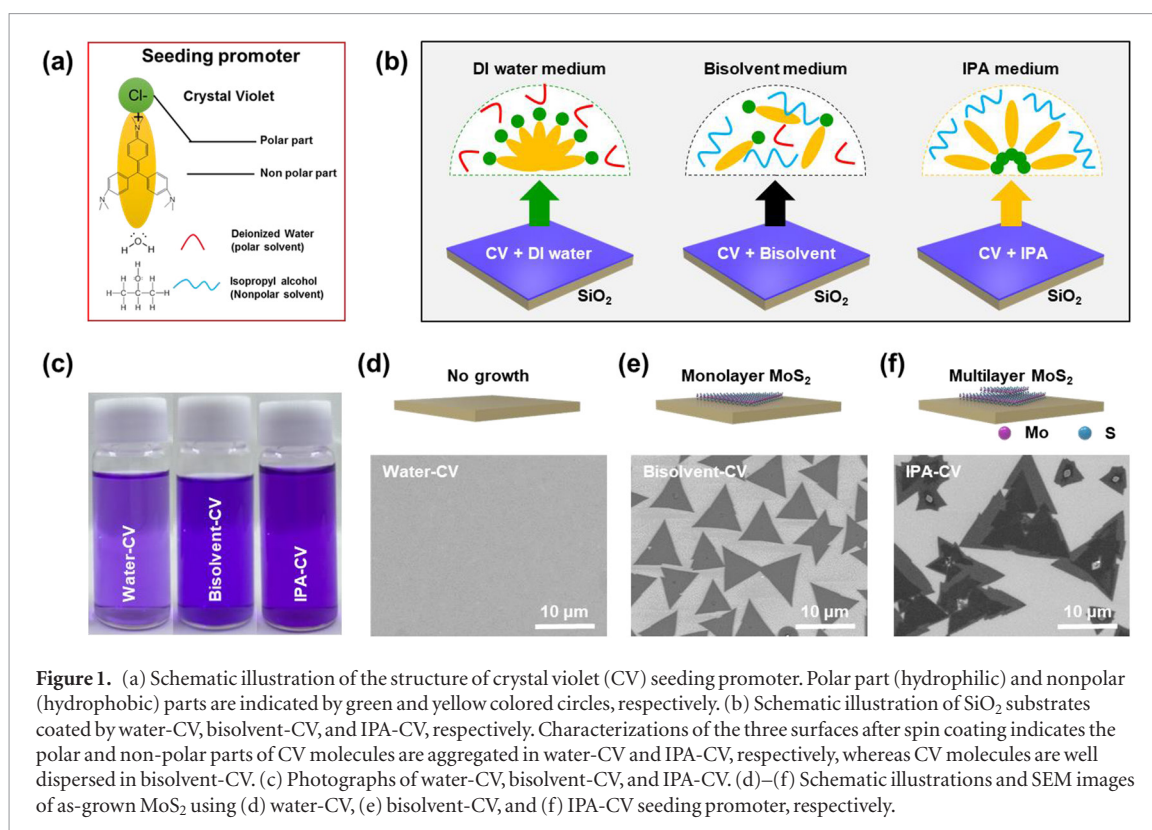
Figure 1. (a) Schematic illustration of the structure of crystal violet (CV) seeding promoter. Polar part (hydrophilic) and nonpolar (hydrophobic) parts are indicated by green and yellow colored circles, respectively. (b) Schematic illustration of SiO$_2$ substrates coated by water-CV, bisolvent-CV, and IPA-CV, respectively. Characterizations of the three surfaces after spin coating indicates the polar and non-polar parts of CV molecules are aggregated in water-CV and IPA-CV, respectively, whereas CV molecules are well dispersed in bisolvent-CV. (c) Photographs of water-CV, bisolvent-CV, and IPA-CV. (d)–(f) Schematic illustrations and SEM images of as-grown MoS$_2$ using (d) water-CV, (e) bisolvent-CV, and (f) IPA-CV seeding promoter, respectively.

used as precursors, separately placing at upstream and adjacent front of the growth substrate (figure S2, supplementary information). Temperatures of two zones at S powder and MoO$_3$ film/growth substrate regions were increased to 180 °C and 680 °C, respectively (see Method for details), while supplying Ar gas at a flow rate of 350 sccm. Subsequently, MoS$_2$ growth was carried out at 680 °C. When we perform only thermal annealing at this temperature, noticeable water-CV on SiO$_2$ surface was not observed. On the other hand, bisolvent-CV and IPA-CV left smooth stains and a few particles on SiO$_2$ surface, respectively (figures S1(d)–(f), supplementary information). This indicates that lots of CV are evaporated over the melting point of CV (205 °C), and as discussed above the anchoring of CV micelles is particularly weak in the water-CV case. Regarding the actual MoS$_2$ growth, from the scanning electron microscopy (SEM) measurement, we confirmed that MoS$_2$ does not growth on the surface of water-CV (figure 1(d)). On the other hand, as shown in figures 1(e) and (f). Monolayer MoS$_2$ domains predominantly grew on bisolvent-CV surface and multi-layered MoS$_2$ domains were found on IPA-CV surface, respectively (see also figures S1(g)–(i), supplementary information). The size of monolayer and multilayer MoS$_2$ domains ranged from 5 to 20 μm with an average of 8 and 12 μm, respectively.

To analyse difference in the physical and optical properties of monolayer and multilayer MoS$_2$ domains, several measurements were employed. After transfer of both MoS$_2$ samples onto SiO$_2$/Si substrate using PMMA method, clean surface morphologies were observed as shown in SEM and atomic force

microscopy (AFM) images (figures 2(a), (e) and (b), (f), respectively). It is worth noting that the white dots located in the centre of all multilayer MoS$_2$ domains as shown in figure 1(f) disappeared, indicating that residual coagulated CV molecules were dissolved during the wet-transfer process. Height profiles along white-dashed lines in AFM images of figures 2(b) and (f) demonstrated that the thickness of each MoS$_2$ single layer is around ~0.7 nm, which is in a good agreement with a previous report [36]. In addition, measuring the Raman spectra of monolayer and multilayer MoS$_2$, E_{2g}^1 and A_{1g} phonon modes near 380 and 400 cm^{-1}, respectively, were clearly observed (figures 2(d) and (h)). The distance between E_{2g}^1 and A_{1g} peaks is sensitive to the number of layers due to the van der Waals interlayer coupling, Coulombic interactions, and stacking-induced changes of intralayer bonding [37]. The E_{2g}^1 and A_{1g} peak distances of 19.8 and 25.8 cm^{-1} for the monolayer and multilayer MoS$_2$ domains, respectively, are in a good agreement with those from previous reports [16, 19], confirming monolayer and thick MoS$_2$ layers. The full width half maximum (FWHM) values of E_{2g} peak, which is one of the indicators for the quality of MoS$_2$, were obtained to be 3.3 and 4.0 cm^{-1} for monolayer and multilayer MoS$_2$, respectively. These values are similar to previously reported FWHM values of CVD-grown MoS$_2$ (3.3 cm^{-1} ~ 7.0 cm^{-1}), implying that the quality of MoS$_2$ is comparable with typical CVD-grown MoS$_2$ [38].

Chemical state and work function of MoS$_2$ domain were evaluated by x-ray photoelectron spectroscopy (XPS) and ultraviolet photoelectron spectroscopy (UPS). Characteristic peaks of Mo 3d$_{3/2}$ (at 232.3 eV),
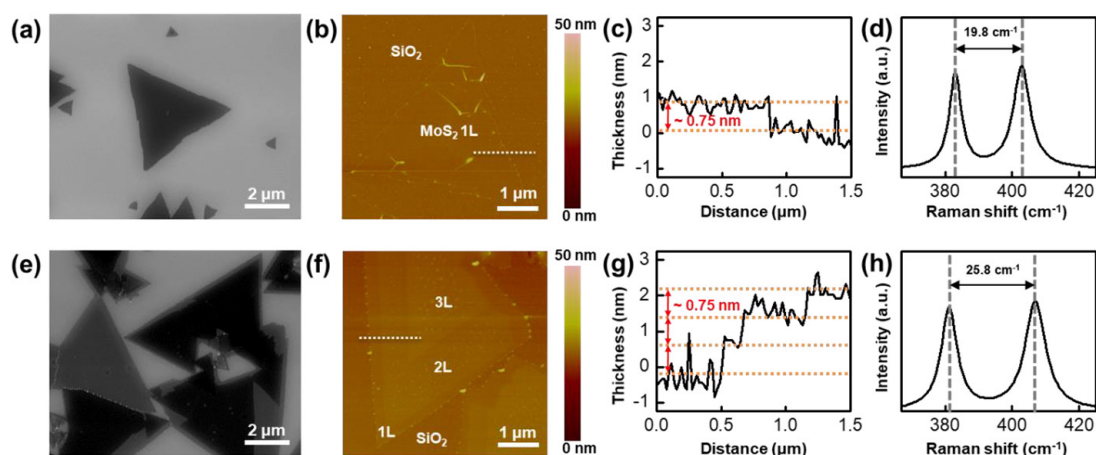
Figure 2. (a) and (e) SEM and (b) and (f) AFM images of transferred (a) and (b) monolayer and (e) and (f) multilayer MoS$_2$ domains grown by (a) and (b) bisolvent-CV and (e) and (f) IPA-CV seeding promoter. (c) and (g) AFM height profile corresponding to the white-dashed line in (b) and (g). Raman spectra of (d) monolayer and (h) multilayer MoS$_2$ domains are shown. Energy differences between two MoS$_2$ Raman modes are 19.8 cm^{-1} and 25.8 cm^{-1}, respectively.
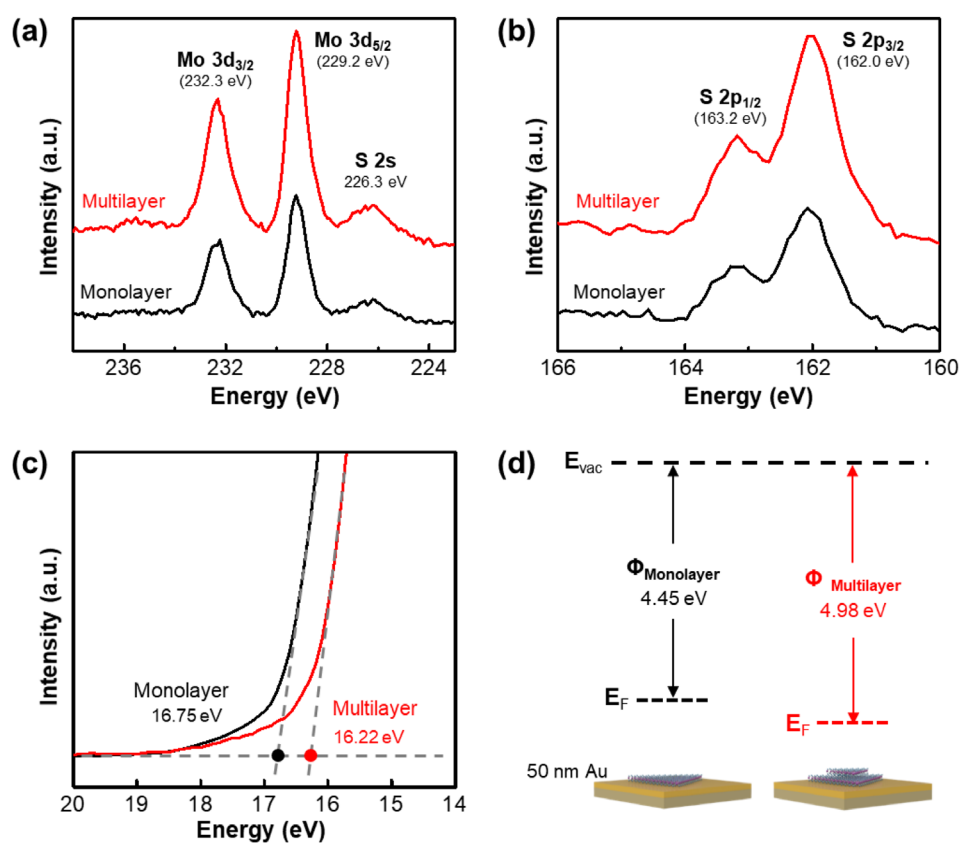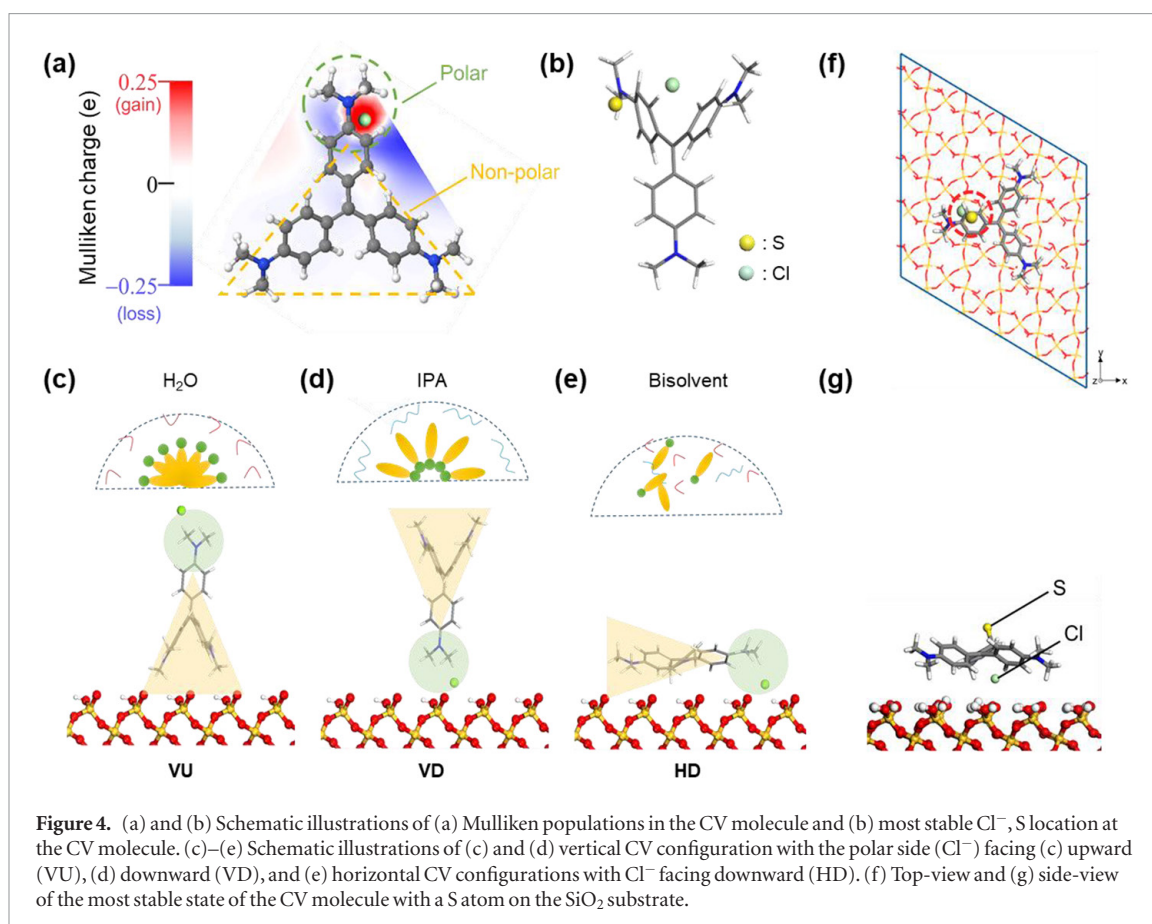

Figure 3. (a) Mo 3d and (b) S 2p XPS core level spectra of monolayer and multilayer MoS$_2$ domains. (c) UPS spectra of monolayer and multilayer MoS$_2$ domains. Inelastic high-binding-energy cutoffs are 16.75 eV and 16.22 eV for monolayer and multilayer domains, respectively. (d) Work function variations of monolayer and multilayer MoS$_2$ domains determined according to $\Phi = h\nu - (E_{cutoff} - E_F)$, where $h\nu$, E_F, and E_{cutoff} are the UPS spectra-derived excitation photon energy, Fermi level edge, and inelastic high-binding-energy cutoff, respectively.

Mo 3d$_{5/2}$ (at 229.2), S 2S (at 226.3 eV), S 2p$_{1/2}$ (at 163.2 eV), an S 2p$_{3/2}$ (at 162.0 eV) in the XPS core level spectra of Mo 3d and S 2p for monolayer and multilayer MoS$_2$ domains were clearly observed (figures 3(a) and (b)) [16]. Any peaks related to molybdenum oxide or metal sulphate were not detected. Moreover, XPS spectra for monolayer and multilayer MoS$_2$ domains

were almost identical. These results further support that well-defined MoS$_2$ domains are grown with similar chemical states. On the other hand, work functions (Φ) of monolayer and multilayer MoS$_2$ domains (denoted as $\Phi_{Monolayer}$ and $\Phi_{Multilayer}$, respectively) were measured by ultraviolet photoelectron spectroscopy (UPS). The work function Φ was determined from

Figure 4. (a) and (b) Schematic illustrations of (a) Mulliken populations in the CV molecule and (b) most stable Cl⁻, S location at the CV molecule. (c)–(e) Schematic illustrations of (c) and (d) vertical CV configuration with the polar side (Cl⁻) facing (c) upward (VU), (d) downward (VD), and (e) horizontal CV configurations with Cl⁻ facing downward (HD). (f) Top-view and (g) side-view of the most stable state of the CV molecule with a S atom on the SiO₂ substrate.

$\Phi = h\nu - (E_{\text{cutoff}} - E_{\text{F}})$, where $h\nu, E_{\text{F}},$ and E_{cutoff} are the excitation photon energy of 21.2 eV, Fermi level edge of 0 eV in this work, and inelastic high-binding-energy cutoff, respectively [39]. The E_{cutoff} was obtained from the linear extrapolation of inelastic high-binding-energy cutoff of samples (figure 3(c)). As schematically summarized in figure 3(d), the obtained Φ value of monolayer MoS₂ domains is 4.45 eV, and is smaller than that of multilayer MoS₂ domains (4.98 eV). A similar trend of increasing Φ value with increasing MoS₂ thickness was previously observed in Kelvin probe force microscopy measurement, and was attributed to the reduction of interlayer screening effect with increasing layer thickness [40].

To further elucidate the role of seeding promoter CV in MoS₂ growth, we performed DFT calculations. Considering first the equilibrium configuration of triangular-shaped CV molecule, we found that the Cl⁻ ion is electrostatically stabilized next to one of the three N⁺ sites within the CV base (figure S3 and table S1, supplementary information) [41, 42]. This placement of Cl⁻ breaks the D₃ symmetry of CV base and constitutes the polar part of CV. The spatial distribution of CV polarity identified according to Mulliken population charges are displayed in figure 4(a) [43]. Next, we consider the initial step of MoS₂ nucleation by exploring the adsorption of S or Mo atoms onto CV (figure S4, supplementary information). Considering the binding of a Mo atom to CV, we observed that the Mo atom is too strongly bound to CV and significantly distorts or destroys CV. Consequently, the initial Mo

binding to CV was excluded from the possible scenario for the experimentally observed high-quality MoS₂ growth (figure S5 and table S2, supplementary information). Considering the binding of a S atom to CV, we then find that the S atom is preferably bound to the polar part of CV, and particularly the most favourable S-CV binding is achieved when Cl⁻ and S are located at the opposite sides of the CV base plane (figure 4(b); see also figure S6 and table S2, supplementary information).

With the understanding of the S-CV as the initial step of MoS₂ growth, we now take into account the effect of the SiO₂ surface. In experiments, by varying the polarity of the various solvent medium, different configurations of CV on SiO₂ were induced. In view of this agenda, four representative CV-SiO₂ configuration models were considered (figures 4(c)–(e)): standing-up or vertical CV configurations with the polar side (where Cl⁻ was located) facing upward (VU) or downward (VD), and lying-down or horizontal CV configurations with Cl⁻ facing upward (HU) or downward (HD). Note that the VU and VD configurations correspond to the water and IPA solvent cases, respectively, while the HU/HD configurations could be associated with the bisolvent medium (figure 1(b)). Specifically, the VU and VD conformations results from the unzipping of CV micelles and their adsorption on SiO₂ as interfacial monolayers. In forming a monolayer from water-CV (figure 1(b) middle panel and supplementary information figure S1(a)), the polar part of CV is exposed to water while the non-polar part binds

to the SiO$_2$ surface (VU configuration; figure 4(c)). In this case, the calculated CV-SiO$_2$ adsorption energy was −0.97 eV (table S3, supplementary information), too weak to provide a stable framework for MoS$_2$ growth at the high experimental growth temperature. The CV molecules desorbed from the SiO$_2$ surface will then evaporate due to their low melting point of 205 °C, which explains well the experimental observation of no noticeable MoS$_2$ growth.

On the other hand, in forming an interfacial monolayer from IPA-CV (figure 1(b) right panel and supplementary information figure S1(c)), the non-polar part of CV is exposed to IPA medium and the polar part contacts the SiO$_2$ surface (VD configuration; figure 4(d)). The calculated CV-SiO$_2$ adsorption energy was increased to −1.71 eV (table S3, supplementary information), which should enable the MoS$_2$ growth at high temperature. The concentrated CV polar parts within monolayers then should provide coagulated S binding sites or induce multiple nucleation of MoS$_2$, explaining the experimental observations of multilayer MoS$_2$ growth. Here, rough morphology of realistic amorphous SiO$_2$ surface will likely result in a disordered self-assembly of standing-up CV molecules [44, 45], further contributing to non-uniform initial growth that leads to multilayer formation of MoS$_2$.

Moving to the bisolvent medium case, CV molecules are originally present in isolation within the solvent and will thus individually adsorb on the SiO$_2$ surface in lying-down configurations (figure 1(b) middle panel and supplementary information figure S1(b)). We then find that this will significantly strengthens the CV-SiO$_2$ binding (table S3, supplementary information), obtaining the adsorption energies of −3.90 eV and −3.20 eV for the HD and HU configurations, respectively. These strong CV-SiO$_2$ interactions will prevent the desorption or re-aggregation of CVs at high temperature. Regarding the preference of the HD configuration over its HU counterpart, the tendency results from the strengthening of CV binding to the SiO$_2$ surface through the Cl$^-$ ion sandwiched between the CV base and SiO$_2$ (figure 4(e)). The CV HD configuration should then naturally promote the nucleation for MoS$_2$ growth by exposing the most favourable S binding sites toward depositing S atoms (figure 4(b)) and at the same time maintaining a strong CV-SiO$_2$ adsorption (figure 4(e)). Explicitly scanning for the favourable S adsorption site, we indeed confirmed that the S adsorption is stabilized by forming a Cl$^-$-CV base-S complex with the angle between the SiO$_2$ surface and the ring plane of CV of ~20° as shown in figure 4(g) (figure S7 and table S4, supplementary information). We thus conclude that the polar part in CV serves several purposes by providing the nucleation site for the growth of MoS$_2$ and concurrently increasing the strength of CV binding onto SiO$_2$ surface. Overall, our results indicate that the coexistence of polar and nonpolar parts in aromatic seed molecules is beneficial for the growth of high-quality monolayer

MoS$_2$ at high temperature, which may explain why PTAS consisted of two polar parts at each edge of the perylene and nonpolar part of perylene is a good seed promoter [31].

3. Conclusion

In summary, we systematically studied the role of the seeding promoter in the CVD growth of MoS$_2$ by employing the CV molecule. To understand the roles of polar and nonpolar parts of CV in the MoS$_2$ growth, the CV configuration on the SiO$_2$ surface was engineered by using solvents with different polarity. Multilayer MoS$_2$ domains were grown from coagulated standing-up CV configurations, whereas monolayer MoS$_2$ domains were predominantly synthesized from randomly distributed lying-down CV configurations. First-principles calculations revealed that the nucleation of MoS$_2$ begins from the S adsorption on the polar part of CV by forming the S-CV base-Cl$^-$ complex, explaining the growth of multilayer MoS$_2$ domains from coagulated standing-up CV configurations with concentrated polar parts contacting the rough SiO$_2$ surface. On the other hand, it was found that the lying-down CV configuration not only provides an ideal configuration for the S adsorption but also achieves stronger CV-SiO$_2$ interactions. Thus, randomly distributed lying-down CV configurations, particularly with Cl$^-$ placed between the CV base and SiO$_2$ surface should provide preferable conditions for the growth of high-quality monolayer MoS$_2$. Given the microscopic understanding on the effects of CV configurations on the SiO$_2$ surface and the multiple roles of polar CV parts for the MoS$_2$ growth, our combined experimental and theoretical considerations not only provide a general framework to understand the growth of monolayer MoS$_2$ from diverse aromatic seeding promoters [31, 46], but also open up new avenues for designing seeding promoters.

4. Experimental section

4.1. Synthesis of MoS$_2$ using crystal violet seeding promoter

As a seeding promoter, 125 mg of crystal violet (⩾90.0%, anhydrous basis, Sigma-Aldrich) was dissolved in 50 ml of DI water, bisolvent, and IPA, respectively. A silicon substrate with a 300 nm SiO$_2$ layer was cleaned by sonication in acetone for 20 min. After sonication, the SiO$_2$/Si substrate was cleaned by acetone, ethanol, and isopropyl alcohol (IPA). Prior to the coating of seeding promoter solution, the cleaned SiO$_2$/Si substrate was positioned under a UV ramp for 10 min to make hydrophilic surface. Seeding promoter solutions were coated on the SiO$_2$/Si substrate at 3000 rpm for 30 seconds. To evaporate solvent residues, CV-coated substrate was dried on a hot plate at 80 °C for 60 s.

For the synthesis of MoS$_2$, a 1-inch quartz tube was equipped with two furnaces (figure S2, supplemen-

tary information). As a sulfur precursor, an alumina boat containing 200 mg of sulfur powder was placed in the upstream furnace (furnace zone 1) while 50 nm-thick MoO_3 thin film deposited on $5 \times 5\,mm^2$ piece of alumina by using thermal evaporator (Thermal evaporation, Woosung Hivac) and a CV-coated SiO_2/Si substrate were positioned on the downstream furnace (furnace zone 2). The quartz tube was purged by 1000 sccm of high purity argon for 5 min. After purging, temperatures of furnace zone 1 and zone 2 were ramped to 180 °C (~15 °C min^{-1}) and 680 °C (~32.5 °C min^{-1}), respectively, under Ar atmosphere at a flow rate of 350 sccm. These temperatures were maintained for 30 min and then naturally cooled down to the room temperature. The entire growth process was carried out under argon atmosphere at a flow rate of 350 sccm.

4.2. Characterization methods

Surface morphologies of CV-coated SiO_2/Si substrates and as-grown MoS_2 were analyzed by optical microscopy (Eclipse LV150, Nikon), scanning electron microscopy (Nova NanoSEM 450, FEI company), and atomic force microscopy (Dimension 3, Veeco). The thickness and the crystal quality of as-grown MoS_2 flakes were characterized by Raman spectroscopy with ~1 μm size of beam (inVia confocal Raman microscope, Renishaw) and Photoluminescence system (MicOS, Horiba) with 514 nm and 532 nm wavelength lasers, respectively. To avoid damages of MoS_2, Raman and PL measurements were performed with <0.1 μW. For the analysis of the thickness and the chemical state, as-grown MoS_2 flakes were transferred to other SiO_2/Si substrates and 50 nm thick Au substrates via PMMA mediated wet transfer method [18]. Chemical states and work functions of monolayer and multilayer MoS_2 domains were analyzed by x-ray photoelectron spectroscopy and ultraviolet photoelectron spectroscopy (K-Alpha and ESCALAB Xi, Thermo scientific) measurements, respectively. Monochromatic Al-Kα (1486.6 eV, for XPS) and He I (21.2 eV for UPS: ~10 mm beam spot size in a diameter) sources were used as photon and ultraviolet sources, respectively.

4.3. Theoretical calculations

To study the adsorption of a S or Mo atom on CV, we adopted an isolated CV molecule composed of two parts, methylrosanilide (CV base) and chloride ion (Cl^-). To study the adsorption of a S atom onto the CV placed on the silica substrate, a SiO_2 model was based on the crystalline α-quartz structure was prepared [44, 47]. Using a slab model made of two (0 0 0 1)-direction α-quartz SiO_2 unit layers and passivating the surface dangling bonds with hydrogen atoms, we constructed a 5×5 hexagonal supercell (lattice constant 2.52 nm) and relaxed the topmost SiO_2 layer (figure S7, supplementary information). A 20 Å of supercell

vacuum was introduced along the SiO_2 surface-normal direction to avoid artificial interactions with periodic images.

Spin-polarized DFT calculations were carried out using the SIESTA code [48]. We adopted Perdew-Burke-Ernzerhof parameterization of generalized gradient approximation augmented by the van der Waals correction proposed by Grimme (DFT-D2) [49, 50]. The core electrons were replaced by Troullier-Martins-type norm-conserving pseudopotentials [51], and wavefunctions were described by double-ζ-plus-polarization level of numerical atomic basis sets with confinement energy of 80 meV. Real-space integration was performed with a mesh cut-off energy of 300 Ry, and only the Γ-point of the Brillouin zone was sampled. All ground-state geometries were obtained by minimizing ionic forces until they all converge below 0.02 eV Å^{-1}. Adsorption energies (ΔE_{ads}) were calculated with the follwoing equation:

$$\Delta E_{ads} = \Delta E_{total} - \Delta E_{substrate} - \Delta E_{adsorbate} \quad (1)$$

where ΔE_{total}, $\Delta E_{substrate}$ and $\Delta E_{adsorbate}$ are the total energies of the substrate-adsorbate complex, substrate and adsorbate, respectively. Corresponding electronic structure changes were analyzed by the charge density difference and Mulliken population [43, 52].

Supplementary information

Additional experimental result, detailed growth condition, and theoretical calculation results are included in the supplementary information.

ORCID iDs

Yong-Hoon Kim ⬦ https://orcid.org/0000-0001-5209-4908
Soo Min Kim ⬦ https://orcid.org/0000-0003-1008-6744

References

[1] Li X and Zhu H W 2015 *J. Materiomics* **1** 33

[2] Wang Q H, Kalantar-Zadeh K, Kis A, Coleman J N and Strano M S 2012 *Nat. Nanotechnol.* **7** 699

[3] Chen H W, Li J Y, Chen X Z, Zhang D and Zhou P 2018 *Semicond. Sci. Technol.* **33** 024011

[4] Tsai M L, Su S H, Chang J K, Tsai D S, Chen C H, Wu C I, Li L J, Chen L J and He J H 2014 *ACS Nano* **8** 8317

[5] Wang W, Panin G N, Fu X, Zhang L, Ilanchezhiyan Z P, Pelenovich V O, Fu D J and Kang T W 2016 *Sci. Rep.* **6** 31224

[6] Perera M M, Lin M W, Chuang H J, Chamlagain B P, Wang C Y, Tan X B, Cheng M M C, Tomanek D and Zhou Z X 2013 *ACS Nano* **7** 4449

[7] Podzorov V, Gershenson M E, Kloc C, Zeis R and Bucher E 2004 *Appl. Phys. Lett.* **84** 3301

[8] Kim S *et al* 2012 *Nat. Commun.* **3** 1011

[9] Radisavljevic B, Radenovic A, Brivio J, Giacometti V and Kis A 2011 *Nat. Nanotechnol.* **6** 147

[10] Wang J L *et al* 2016 *Adv. Mater.* **28** 8302

[11] Coleman J N *et al* 2011 *Science* **331** 568

[12] Fu D Y *et al* 2017 *Chem. Soc.* **139** 9392

[13] Smith R J *et al* 2011 *Adv. Mater.* **23** 3944

[14] Tan L K, Liu B, Teng J H, Guo S F, Low H Y, Tan H R, Chong C Y T, Yang R B and Loh K P 2014 *Nanoscale* **6** 14002

[15] Sun D, Nquyen A E, Barroso D, Zhang X, Preciado E, Bobek S, Klee V, Mann J and Bartels L 2015 *2D Mater.* **2** 045014

[16] Choi S H, Stephen B, Park J H, Lee J S, Kim S M, Yang W and Kim K K 2017 *Sci. Rep.* **7** 1983

[17] Shi Y M *et al* 2012 *Nano Lett.* **12** 2784

[18] Lee Y H *et al* 2012 *Adv. Mater.* **24** 2320

[19] Boandoh S *et al* 2017 *Small* **13** 1701306

[20] Tao L, Chen K, Chen Z F, Chen W J, Gui X C, Chen H J, Li X M and Xu J B 2017 *ACS Appl. Mater. Interfaces* **9** 12073

[21] Zhan Y J, Liu Z, Najmaei S, Ajayan P M and Lou J 2012 *Small* **8** 966

[22] Liu K K *et al* 2012 *Nano Lett.* **12** 1538

[23] Ji Q Q *et al* 2013 *Nano Lett.* **13** 3870

[24] Yan A M, Velasco J, Kahn S, Watanabe K, Taniguchi T, Wang F, Crommie M F and Zettl A 2015 *Nano Lett.* **15** 6324

[25] Ahmed K B A and Anbazhagan V 2017 *RSC Adv.* **7** 36644

[26] Faber M S, Lukowski M A, Ding Q, Kaiser N S and Jin S 2014 *J. Phys. Chem.* C **118** 21347

[27] American Society for Metals and National Bureau of Standards 1980 *Bulletin of Alloy Phase Diagrams* (Metals Park, OH: American Society for Metals) p 11

[28] Yun S J *et al* 2015 *ACS Nano* **9** 5510

[29] Shi J P *et al* 2015 *Adv. Funct. Mater.* **25** 842

[30] Kang K, Xie S E, Huang L J, Han Y M, Huang P Y, Mak K F, Kim C J, Muller D and Park J 2015 *Nature* **520** 656

[31] Ling X, Lee Y H, Lin Y X, Fang W J, Yu L L, Dresselhaus M S and Kong J 2014 *Nano Lett.* **14** 464

[32] Kim K K, Hsu A, Jia X T, Kim S M, Shi Y M, Dresselhaus M, Palacios T and Kong J 2012 *ACS Nano* **6** 8583

[33] Gao L B, Ren W C, Zhao J P, Ma L P, Chen Z P and Cheng H M 2010 *Appl. Phys. Lett.* **97** 183109

[34] Yang P *et al* 2019 *Nano Res.* **12** 823

[35] Lee J H *et al* 2007 *J. Phys. Chem.* C **111** 2477

[36] Zhang H Li Q, Yap C C R, Tay B K, Edwin T H T, Olivier A and Baillargeat D 2012 *Adv. Funct. Mater.* **22** 1385

[37] Lee C, Yan H, Brus L E, Heinz T F, Hone J and Ryu S 2010 *ACS Nano* **4** 2695

[38] Xu X, Das G, He X, Hedhili M N, Fabrizio E D, Zhang X and Alshareef H N 2019 *Adv. Funct. Mater.* **29** 1901070

[39] Kim J H, Lee J, Kim J H, Hwang C C, Lee C and Park J Y 2015 *Appl. Phys. Lett.* **106** 251606

[40] Choi S, Shaolin Z and Yang W 2014 *J. Korean Phys. Soc.* **64** 1550

[41] Cañamares M V, Chenal C, Birke R L and Lombardi J R 2008 *J. Phys. Chem.* C **112** 20295

[42] Meng W, Hu F, Zhang L-Y, Jiang X-H, Lu L-D and Wang X 2013 *J. Mol. Struct.* **1035** 326

[43] Kim H S, Kim H S, Kim S S and Kim Y-H 2014 *Nanoscale* **6** 14911

[44] Koch N 2012 *Phys. Status Solidi* **6** 277

[45] Yu Y J *et al* 2017 *Adv. Mater.* **29** 1603925

[46] Shi Y, Li H and Li L-J 2015 *Chem. Soc. Rev.* **44** 2744

[47] Kang J, Kim Y-H, Bang J and Chang K J 2008 *Phys. Rev.* B **77** 195321

[48] José M S, Emilio A, Julian D G, Alberto G, Javier J, Pablo O and Daniel S-P 2002 *J. Phys.: Condens. Matter* **14** 2745

[49] Perdew J P, Burke K and Ernzerhof M 1996 *Phys. Rev. Lett.* **77** 3865

[50] Grimme S 2006 *Comput J. Chem.* **27** 1787

[51] Troullier N and Martins J L 1991 *Phys. Rev.* B **43** 1993

[52] Lee J, Cho A E, Kumar S, Jang S S and Kim Y-H 2018 *Adv. Funct. Mater.* **28** 1706970